A core–shell TiON–C nanostructure as a self-supported and scalable electrode for fast oxygen evolution reaction in acidic media

Journal of Physics: Energy

OPEN ACCESS

RECEIVED
21 July 2025

ACCEPTED FOR PUBLICATION
22 September 2025

PUBLISHED
9 October 2025

PAPER

A core–shell TiON–C nanostructure as a self-supported and scalable electrode for fast oxygen evolution reaction in acidic media

Federico Baiutti[1,2,*], **Kosova Kreka**[1], **Aleš Marsel**[2], **Miha Hotko**[2], **Marjan Bele**[2], **Anja Logar**[2], **Martin Šala**[5], **Črtomir Donik**[3], **Lazar Bijelić**[2], **Carolina Duque Serra**[1], **Alex Morata**[1], **Albert Tarancon**[1,4], **Miran Gaberscek**[2] and **Nejc Hodnik**[2,3]

[1] Department of Advanced Materials for Energy Applications, Catalonia Institute for Energy Research (IREC), Jardins de les Dones de Negre 1, 08930 Sant Adrià del Besòs, Barcelona, Spain
[2] Department of Materials Chemistry, National Institute of Chemistry, Ljubljana SI-1000, Slovenia
[3] Institute of Metals and Technology, Ljubljana 1000, Slovenia
[4] Catalan Institution for Research and Advanced Studies (ICREA), Passeig Lluís Companys 23, 08010 Barcelona, Spain
[5] Department of Analytical Chemistry, National Institute of Chemistry, Ljubljana SI-1000, Slovenia
[*] Author to whom any correspondence should be addressed.

E-mail: fbaiutti@irec.cat

Keywords: PEMEC, fuel cells, hydrogen, titania, iridium, anode

Supplementary material for this article is available online

Abstract

A novel self-supported architecture, based on carbon nanofibers homogeneously coated by an ultrathin TiON layer and functionalized by a fine dispersion of Ir nanoparticles (NPs) with ultralow loading (60 $\mu g * cm^{-2}$ with particle size ≈1.5 nm), is presented as a potential anode for proton exchange membrane electrolysis cells. This structure serves as an ideal anode for rapid electrochemical oxygen evolution reaction in acidic conditions. It combines the high conductivity of the carbon-TiON core–shell structure, the chemical stability of the TiON thin layer to protect C against corrosion, and the enhanced mass activity of Ir NPs. Additionally, it offers excellent mechanical stability and a straightforward, scalable fabrication process. The electrochemical activity (80 mA cm^{-2}/1.2 mA $* \mu g_{Ir}{}^{-1}$ @ 1.6 V) outperforms C–Ir and Ir-black references. Preliminary long-term test are carried out and strategies for a potential improvement of the long-term stability are critically discussed.

1. Introduction

The possibility of achieving wide implementation of green hydrogen-based technologies is dependent on the introduction of optimized energy conversion systems that combine efficiency, durability and cost-effectiveness. In the specific context of hydrogen production via electrolysis, low temperature proton exchange membranes electrolysis cells (PEMECs) exhibit a number of technological advantages including rapid system response, large dynamic range of operation and a compact design [1]. However, a major bottleneck in PEMECs is represented by the difficult trade-off between minimization of the kinetic barrier for the oxygen evolution reaction (OER) and long-term stability under operation (high potentials and in acidic environment) [2], which strongly limits the choice of materials and architectures. The typical design of a state-of-the-art (SoA) PEMEC anode is represented by a catalyst layer (CL) made by noble metal particles (Ir/Ru oxide) distributed on top of the electrolytic membrane, and by Ti-based porous transport layer (PTL), which acts as a mechanical support, as an electrical contact for the CL and for facilitating gas/water transport. A typically high loading (1–2 mg $* cm^{-2}$) favors the formation of a percolative network between the noble metal particles, while a sputtered Pt interlayer is often used to improve the electrical contact between CL and PTL [3, 4]. There exists a strong drive for the reduction of Ir loading (by at least a factor 4–5), given the scarcity of the material and the consequent direct impact on the PEMEC capital cost [5, 6].

Improved OER activity has been reported e.g. by employing Ir nanoparticles (NPs), that offer maximized surface/volume ratios and intrinsic catalytic activity enhancement by size effects [7–9]. Moving from a noble metal-based CL to finely dispersed noble metal catalyst particles, however, brings along important drawbacks including tendency to particle aggregation/dissolution and current percolation issues [10]. Focus needs to be put into the optimization of a catalyst-support assembly that meets the demands for particle stabilization, resistance to corrosion and presence of a highly conducting current percolative network [11]. Scalability and straightforward processing should be ensured, too. Considering the poor stability of C-based supports (largely employed for PEM fuel cells) at PEMEC anode working potential and temperatures due to corrosion issues [12–14], alternatives have been sought in the form of conductive oxides (e.g. doped SnO_2-based) [15]. Titania in particular has come to the fore as an effective support material, capable of limiting NP aggregation and of boosting the intrinsic catalyst activity thanks to catalyst-support interaction [16]. Implementing an oxide conductive layer, however, comes at the cost of a potentially reduced electronic conductivity, which may become dramatic when an n-type conductor such as TiO_2 is exposed to a highly oxidative environment such as a PEMEC anode. Numerous efforts have been made to stabilize the conductivity of TiO_2 through doping [17–19]. For example, Bele *et al* developed a dimensionally stable anode based on a nanotubular titanium oxynitride support for Ir NP by simple anodization process exhibiting high OER activity (>2 mA * $\mu g_{Ir}{}^{-1}$@1.6 V) and good durability [20]. An interesting hybrid approach is to develop architectures capable of combining the excellent electrical conductivity of C with the high electrochemical stability of TiO_2 [21]. For example, Kim *et al* have recently introduced a layer-by-layer coating method for the fabrication of carbon nanotubes-TiO_2 nanocomposites functionalized by Ir NP, which has been tested in the form of catalyst ink for OER [22]. Alternative C-TiO_2 based nanostructures have been developed [23], including disordered hybrid composites [24], sandwiched structures [25], hollow spheres [26] and mixed nanofibers [27]. When considering these structures for electrocatalysis and OER, however, limitations may be encountered in terms of scalability and reproducibility of the fabrication method, exposure of C to the atmosphere, low mechanical strength and the requirement of an additional support layer.

In the present work, we present a novel anode structure for electrochemical OER, which represents an ideal C-TiO_2 composite by design. It consists of mechanically stable and robust C nanofibers in the form of a cloth, coated by an ultrathin (<50 nm) continuous layer of highly conductive TiON and functionalized by an ultra-low loading of Ir NPs. The support is fabricated via an easy process, utilizing scalable methods that are readily available at the industrial level, namely electrospinning and atomic layer deposition (ALD), followed by NP functionalization via dip-coating. The structure has been tested as a fully self-supported OER anode layer in combination with a Nafion membrane and showed high OER activity.

2. Results and discussion

Large area paper-like fabrics of Ir–C@TiON electrode have been fabricated following the route sketched in figure 1(a). PAN fibers, produced by electrospinning [28], are carbonized at high temperatures in inert atmosphere (cf. experimental section for details), followed by the deposition of a conformal ultrathin coating layer of TiO_2 by ALD. The titania layer is then functionalized by nitridation during annealing in NH_3 atmosphere. Finally, an ultra-fine dispersion of Ir NPs (size $\approx$1 nm, cf. later in the text) is synthesized by dip-coating and thermal treatment, following a recipe developed by our group [29]. Note that all the employed steps are scalable: specifically, electrospinning allows for high flexibility in the fiber with typical thickness ranging from few tens to few hundred microns, and it is an industrially mature fabrication processes capable to produce hundred thousand m^2 per day [30]. Similarly, ALD is considered among the most promising techniques for the large-scale production of thin films at the industrial level [31, 32]. The resulting structure and morphology of the Ir–C@TiON structure, as retrieved by SEM, can be appreciated in figure 1, panels (b)–(g). The C support fabrics present a porous microstructure with a thickness $\approx$30 μm (b). The top-view images in panels (b) and (c) for low and high magnification, respectively, highlight a preferential alignment of the fibers and a highly porous architecture. The high magnification images in panels (d) and (f—close-up of the area indicated by the red rectangle in d) show the fine distribution of Ir NPs on the surface of the fibers. Finally, figure 1(e) shows a cross-section of the C@TiO_2 core–shell structure resulting from the ALD coating and subsequent NH_3 annealing for nitridation, where the conformality and full density of the coating after annealing can be appreciated. Note that the TiO_2 coating thickness can be precisely controlled with nm-resolution by the number of ALD cycles. In supplementary figure 1, SEM-EDX on a cross section of the fibers (TiO_2 not nitridated) confirms the homogeneous distribution of both TiO_2 and Ir along the cross section of the fiber cloth. Interestingly, the resulting cloth-like structure is fully self-supported and mechanically stable, so that it can be utilized as a stand-alone electrode without the need for additional steps such as crunching and deposition on a current collector.

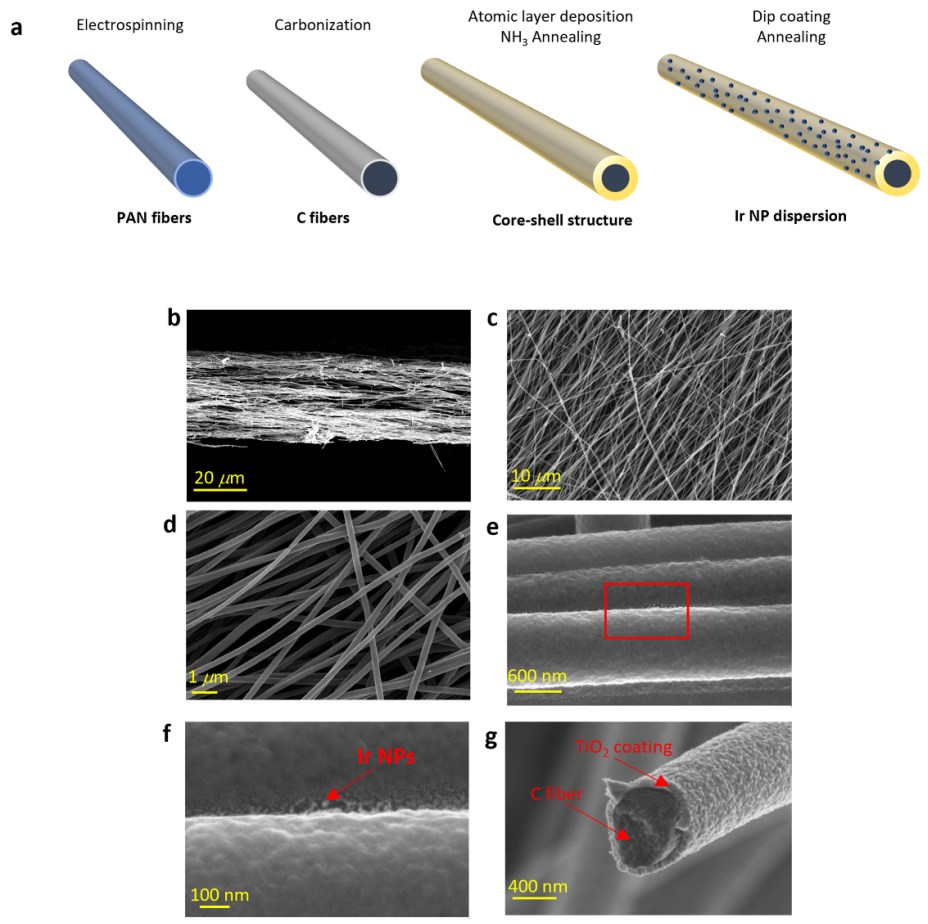

Figure 1. (a) Sketch of the core–shell fabrication process. ((b)–(g)) SEM micrographs for Ir–C@TiON fibers. (b) Fiber cloth cross-section; (c) and (d) top-view low and high magnification, respectively; (e) fiber lateral view; f) magnification of the red rectangle area in panel (d); (g) single fiber cross-section.

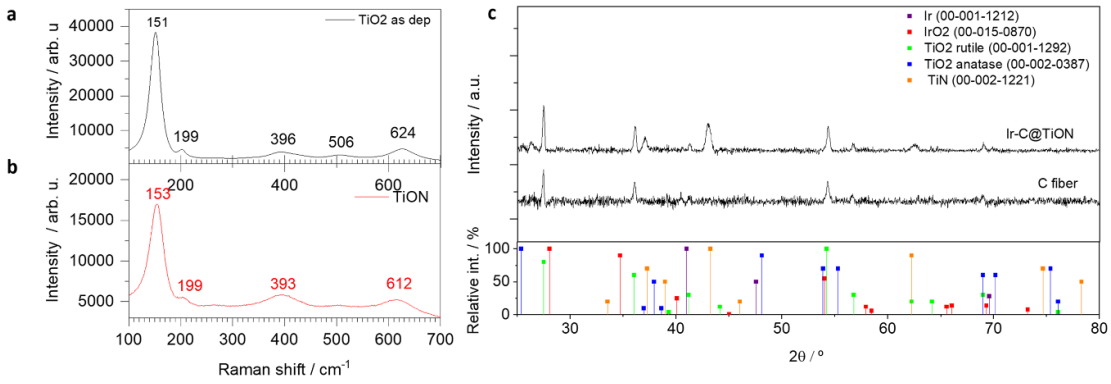

Figure 2. Raman spectra of C@TiON fibers as deposited (a) and after nitridation (b). (c) θ–2θ XRD scan of electrospun C fibers and of the final Ir–C@TiON structure.

In figure 2, the Raman spectra of the TiO_2-coated C fibers, as fabricated and after nitridation, are reported. For the as-deposited material (figure 2(a)), the vibration peaks are around 151 cm^{-1}, 199 cm^{-1}, 396 cm^{-1}, 506 cm^{-1} and 624 cm^{-1}, which are typical of anatase TiO_2 [33, 34]. Successful N incorporation is highlighted by the observed peak shifts after nitridation (figure 2(b)), which are compatible with a change in anion stoichiometry [35]. XRD patterns of the electrode Ir–C@TiON structure and direct comparison with the electrospun C fibers are reported in figure 2(c). There, peaks related to the TiN (e.g. for $2\theta \approx 43°$ and $\approx 62°$) and TiO_2 ($2\theta \approx 70°$) phases, indicating a mixed composition within the Ti(O,N) system, can be identified. No secondary phase peaks are apparent. Owing to the low content and the large peaks overlap, no Ir diffraction peaks can be clearly distinguished.

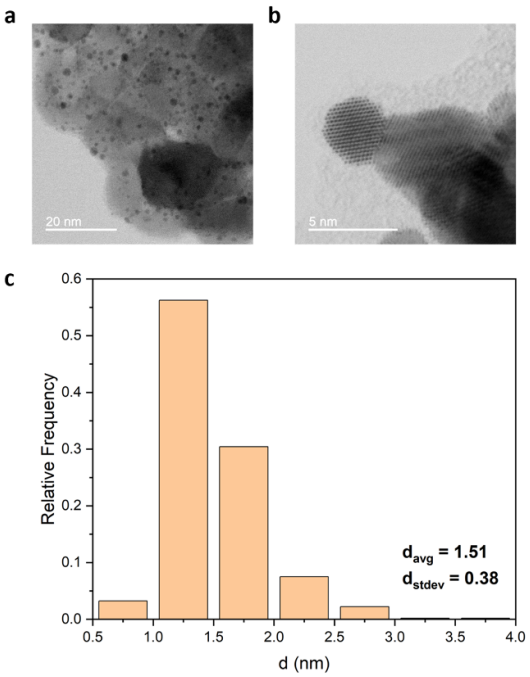

Figure 3. Low- (a) and high-magnification (b) TEM micrographs for Ir NPs on the TiON–C fiber surface. (c) Particle size distribution.

The Ir load was measured by ICP-MS measurement, resulting in 2.1%wt for the specific fiber investigated. This corresponds to a mass load of ≈60 $\mu g * cm^{-2}$, representing a remarkable decrease in the Ir geometrical loading (×15–×30) with respect to SoA PEM electrolyzers [36]. The Ir load was also confirmed by SEM-EDX measurements (supplementary table 1), with values in the range ≈2%–4%wt. depending on the region. One can also observe that the presence of N as a result of TiO_2 nitridation is confirmed. This process is effective for enhancing the electronic conductivity of titania, as demonstrated by the *I–V* curves reported in supplementary figure 2, which result from the measurement of reference TiON dense homogeneous films fabricated using the same procedure on top of sapphire substrates. The material exhibits very high electronic conductivity ≈10^4 S cm^{-1}, in line with literature reports [37]. Note that the resistivity of the as-grown TiO_2 film is >10^3 Ω * cm at room temperature. The conductivity after TiO_2 nitridation (9.3 kS cm^{-1}) is even greater than what achieved by simple reduction (H_2 treatment—5.7 kS cm^{-1}). Based on literature [38, 39], we ascribe this effect to a combined effect of N doping and oxygen vacancy formation (due to the strongly reducing effect of NH_3 annealing), causing Ti^{4+}/Ti^{3+} reduction.

The NP distribution and size was further characterized by TEM, as shown in figure 3. In the low magnification micrograph of figure 3(a), one can observe the fine dispersion of the Ir NPs on the fibers surface, while in figures 3(b)–(a) single particle image is reported, highlighting high crystallinity and a size <5 nm. Statistical analysis highlights an extremely small particle size resulting ≈1–2 nm (figure 3(c)), which ensures maximized material utilization for Ir. By simple geometrical considerations, assuming ≈60% of exposed area (cf. panel (b)), one can estimate an ECSA value of ≈80 $m^2/g_{Ir}{}^{-1}$, in line with previous reports on supported Ir NPs [40]. This can serve as an indication of the electrochemically active area, considering that direct EIS-based approaches are hindered by the double-layer capacitance of the support [20].

In order to test the electrochemical performance of the electrode structure for acidic OER, we built a half cell using used a using a Nafion 115 membrane electrolyte, cold-pressed against the fibers [41]. The structure was mounted in a gas-diffusion electrode (GDE) setup where reference and counter electrode were placed in the top-compartment, which was filled with 0.1 M $HClO_4$ [41]. In this configuration, partial liquid electrolyte penetration through the Nafion membrane [42] ensures good electrode wetting and consequent extension of the electrolyte–electrode contact area along the fiber cross-section. Different TiON coating thicknesses were tested electrochemically: 10 nm, 20 nm, 40 nm. Higher thicknesses have not been considered owing to the duration of the ALD process. The electrochemical activity of Ir–C@TiON is reported in figure 4 (current–voltage curves measured at a scan rate of 20 mV * s^{-1}), in comparison with a Ir–C nanostructure (i.e. C fibers without TiON coating) and with commercial Ir black unsupported catalyst, deposited directly on the Nafion membrane. The first noteworthy observation is related to the enhanced performance of the Ir–C@TiON structure (up to 80 mA * cm^{-2}@1.6 V for the 40 nm-thick

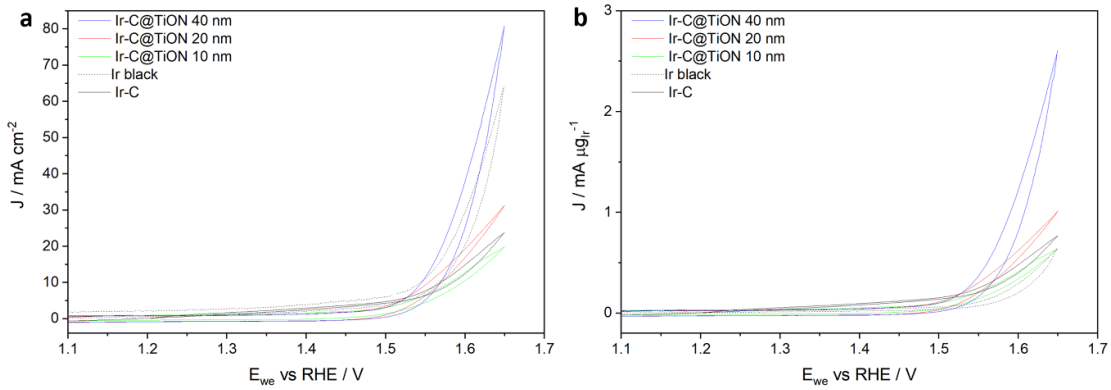

Figure 4. CV curves for Ir–C@TiON with different TiON coating thicknesses, compared to reference Ir black and Ir–C nanofibers. The current density is normalized considering the electrode geometrical area in (a) and the Ir load in (b).

coating—overpotential 320 mV for 10 mA cm^{-2} current density) with respect to the uncoated Ir–C nanostructure (≈15 mA * cm^{-2}@1.6 V), highlighting the key positive effect of TiON in enhancing the Ir OER activity. In a previous publication from our group [20], we demonstrated using DFT simulations that the TiON-Ir interface is characterized by increased adhesion strength, i.e. high stability and low tendency of particle coalescence. Moreover, a beneficial electron transfer is expected at the interface level, which translates into enhanced electrochemical OER kinetics for the catalyst NPs (strong metal support interaction—SMSI). We also note that the activity increases with TiON thickness, possibly do to an improved stability of the coating layer as detailed in the post-mortem analysis (cf. later in the text). While the area specific activity of the Ir–C@TiON structure (40 nm TiO_2) is similar to the Ir-black reference measured in the same conditions, the importance of the ultralow Ir load and particle size that characterizes our nanostructure becomes evident when considering the specific mass activity (figure 4(b)). Here, the current density values exceed 1.2 mA * μg_{Ir}^{-1}@1.6 V, representing a ≈4x enhancement with respect to the Ir-black reference (dotted black line, ≈0.3 mA * μg_{Ir}^{-1}@1.6 V). When comparing to SoA unsupported Ir layers, typical values range between 0.2 mA*μg_{Ir}^{-1}@ 1.65 V and 0.8 mA*μg_{Ir}^{-1}@ 1.6 V [16, 20, 43]. The obtained results are also in line with recent reports on TiO_2-supported Ir NPs. For example Li *et al* proposed a structure based on N-doped TiO_2 powders, achieving an overpotential of 270 mV (10 mA cm^{-2}) for a loading of 300 μg * cm^{-2} [44]. Hu *et al* have reported an overpotential of 200 mV (1 mA cm^{-2}) with a loading of 255 μg * cm^{-2} using a support of Nb-doped TiO_2 NPs [45]. Kim *et al* reported an ALD-based TiO_2-coated carbon support for Ir NPs, thanks to which a mass activity of ≈1 mA * μg_{Ir}^{-1} at 1.55 V was measured [22]. Unlike these studies, however, we highlight that in our case the structure is mechanically self-supported and is characterized by a simple scalable fabrication method. Interestingly, the analysis of the kinetic region (Supplementary figure 3) indicates a high Tafel for both the Ir–C@TiON (≈73 mV dec^{-1}) and the Ir–C (103 mV dec^{-1}). This is higher than what typically reported for Ir-based structures (≈40–50 mV dec^{-1}) [43] and can be tentatively ascribed to a large surface coverage by the intermediate product of the reaction preceding the RDS [46]. This phenomenon can become predominant in our case with respect to 'bulk-like' situations due to the extreme surface/volume ratio, in which a high density of edges/corners can stabilize surface intermediates.

The short-term stability of the structure has been evaluated by a chronopotentiometric (CP) test carried out at 10 mA * cm^{-2} (40 nm TiON coating), as displayed in figure 5. The CV curves (figure 5(a)), obtained at regular intervals during the CP test, indicate a certain stability for 60 mins of operation, followed by a rather substantial decrease after ≈2 h of operation (≈−60% OER current density). The Nyquist plots shown in figure 5(b), recorded at the beginning and at the end of the CP measurement (black and green curve, respectively), have been analyzed to provide some hints into the degradation mechanisms. The impedance spectra are characterized by two well-defined arcs, characterized by distinct time constants, and have been fitted using the equivalent circuit shown in panel (b) [40]. There, a double-layer constant phase element (CPE_{dl}) is in parallel with the charge-transfer resistance (R_{ct}) and the *R–C* component resulting from the intermediates absorption (R_a and C_a, respectively). These circuit elements are in series with the serial resistance R_s, which accounts for the electrolyte resistance and for the electronic conductivity of the fibers. Table 1 reports the best fitting values for the as-fabricated and aged samples. The quality of the fittings can be inferred from the very good overlap between the experimental points and the simulated Nyquist plot in figure 5(b). It is interesting to note that, already in the as-fabricated stage, the impedance is strongly dominated by the electrosorbed intermediate contribution. This may be put in relation to the observed high Tafel slope (cf supplementary figure 3), suggesting a high energy barrier to intermediate absorption possibly

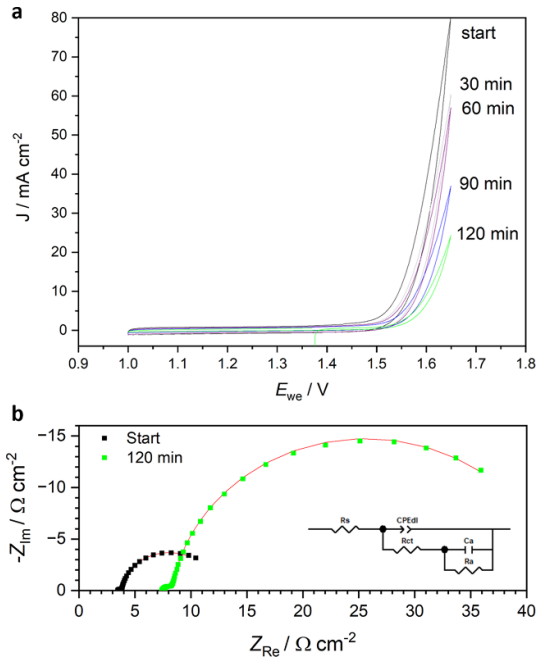

Figure 5. Ageing test for Ir–C@TiON. a) Representative CV curves recorded at regular time interval during chronopotentiometry ageing test @10 mA * cm^{-2}. b) Nyquist plots retrieved at the beginning and at the end of the ageing test (electrode polarization $E_{we} = 1.55$ V). The red line indicates the fitting results, which were achieved using the indicated equivalent circuit.

Table 1. Best fitting values for Ir–C@TiON at the beginning and at the end (120 min) of the CP degradation test.

	R_s/W	Increment/%	C_{dl}/mF	R_{ct}/W	Increment/%	C_a/mF	R_a/W	Increment/%
Start	27.7		0.77	3.2		4.17	67.3	
End	58.9	112.6	0.57	9.6	198.4	1.94	274.9	308.3

as a cause of the specific NP morphology and high surface/volume ratios. This contribution becomes even more prominent during operation, (+308% at the end of the CP test). After degradation, one can also observe—to a lesser extent—an increase in R_{ct} (+198%) and of R_s (+112%).

Although final conclusions on the stability of the developed nanostructures should be drawn only after measurement in more realistic conditions (i.e. at elevated temperatures, where C corrosion is expected to become more relevant), these preliminary data indicate that further optimization is required especially in view of the better stability that has been recently highlighted on similar structures [22]. In order to provide further insights into the degradation processes, post-mortem characterization has been carried out using a suite of characterization tools, namely SEM imaging, SEM-EDX and XPS analyzes. The SEM micrograph of the Ir–C@TiON (40 nm) after CP degradation test is reported in figure 6. There, one can see that the structural integrity of the structure is well-maintained, with the presence of a few isolated cracks and no detachment of the TiON coating. We note that the achievement of such a structural stability is only possible for high TiON thickness, as demonstrated by the SEM characterization of Ir–C@TiON (20 nm) (Supplementary figure 4), showing clear signs of coating delamination. Complementary SEM-EDX results are reported in table 2, in which we compare the elemental atomic ratio between the as-fabricated and aged structures. Notably, the rather constant Ir/Ti ratio before (≈0.14) and after (≈0.11) degradation confirms the structural robustness of the electrode also against Ir dissolution. Next, we turn our attention to the chemical environment, specifically to the Ti oxidation state, using high-resolution (HR) XPS (figure 7). The obtained Ti spectra (before and after degradation, panels (a) and (b), respectively) can be deconvoluted in Ti $2p_{3/2}$ and Ti $2p_{1/2}$ peaks separated by approximately 5.5 eV. In addition to Ti $2p_{3/2}$peak at 458.6 eV of $Ti^{(4+)}$ (e.g. TiO_2) (40%), two other peaks at 457.2 eV (40%) and 456.0 eV (20%), are characteristic for Ti–(O, N) and Ti–N bonding, confirming the partial nitridation of the material in the as-fabricated state. After operation at high potential (panel b), the Ti sum peak changes to one main peak at 458.6 eV–Ti(4+) (75%), with the peaks at 457.2 eV and 456.0 eV decreasing significantly (17% and 8%). This is a strong indication of a re-oxidation process occurring during operation. The logical consequence is the formation of a TiO_2 insulating layer, which prevents electron transfer to the Ir NPs and leads to the observed increased electrode overpotential (R_{ct} and R_a in figure 5), but also in the increased serial contribution (R_s) due to the added

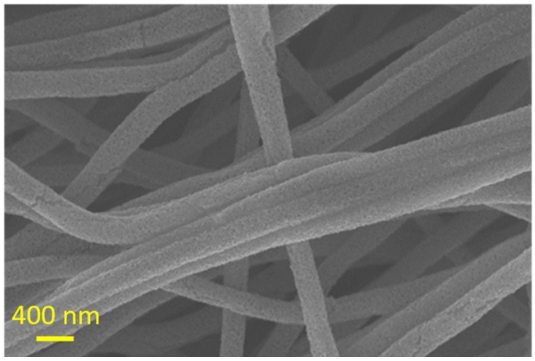

Figure 6. Post-mortem SEM analysis on Ir–C@TiON nanostructures after ageing test.

Table 2. Elemental weight ratio of Ir–C@TiON for structures as fabricated and after degradation tests, measured on different areas by SEM-EDX.

	Before—area1	Before—area 2	Before—area 3	After—area 1	After—area 2	After—area 3
Ir/Ti	0.14	0.14	0.17	0.097	0.11	0.12

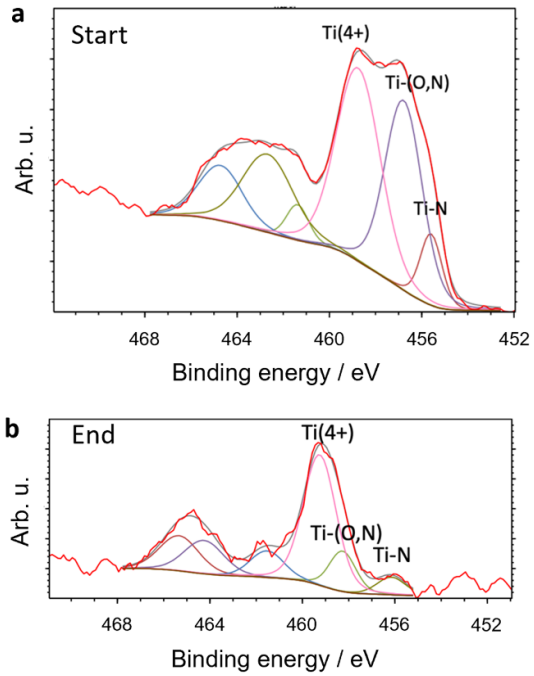

Figure 7. XPS spectra of the Ti2p peak, before (a) and after (b) degradation.

electrical resistance. Interestingly, in a recent study by our group on an Ir NPs-nanotubular TiON structure [20], a similar observation of TiON re-oxidation during operation was found to be independent from the long-term performance. We attribute this difference to morphological effects and specifically to the very low TiON thickness employed in the present work, which provides a relatively short diffusion pathway for oxygen to diffuse in the whole layer leading to complete oxidation and formation to a fully insulating layer. Moreover, the singular contact points between the fibers can be characterized by current striction effects, i.e. by local potential built-up causing the early formation of insulating TiO_2 islands.

These findings also indicate a potential path for improving the stability of the developed electrode, which can be achieved by ensuring long-term conductivity of the titania phase under OER conditions. This can be obtained, for example, by modifying the doping strategy—such as introducing A-site donor doping in TiO_2 (e.g. Nb doping). In this case, the electron concentration (i.e. the Ti^{3+} fraction) is determined by the amount of donor dopant rather than by oxygen stoichiometry or nitrogen content. As a result, it remains unaffected by changes in the anion sublattice caused by oxygen diffusion or nitrogen release, which can occur even at

room temperature under applied bias. Recent literature reports indeed provide indication of superior stability for Nb-doped TiO_2 with respect to the undoped counterpart [18, 47]. We note, however, that technological limitations within the ALD process make this approach not straightforward at the present times.

3. Conclusion

We presented a novel nanostructured electrocatalyst for the OER in acidic environments, composed of core–shell carbon nanofibers fully coated with an ultrathin (10–40 nm) layer of nitrogen-doped TiO_2 and functionalized with small Ir NPs (≈1.5 nm) at an ultralow loading (≈60 μg cm^{-2}). This architecture combines the high electronic conductivity of the carbon core and TiON shell with the high specific activity of Ir NPs, further enhanced by strong TiON–Ir catalyst–support interactions. Electrochemical testing using a realistic GDE setup with Nafion electrolyte demonstrates outstanding activity, achieving up to 80 mA cm^{-2} at 1.6 V and a mass activity of ≈1.2 mA $\mu g_{Ir}{}^{-1}$—over four times higher than the uncoated Ir–C counterpart and surpassing the Ir-black benchmark. While long-term testing reveals some activity loss, post-mortem analysis attributes this to TiO_2 reoxidation. Nonetheless, this nanostructure offers several advantages over SoA OER anodes, including enhanced mechanical stability, efficient use of critical raw materials, protection of the carbon core from corrosion, and high electronic conductivity. The fabrication process is readily scalable, and the system is tunable via modifications to the coating and catalyst composition. Further improvements—such as exploring alternative coating doping strategies—could provide a viable path toward enhanced long-term stability.

4. Experimental

PAN fibers were produced by electrospinning (Nanotechnology Solutions, Yflow) and subsequently carbonized by a two-step process. First, an annealing at 270 °C (17 h) in air was carried out in order to remove hydrogen; afterwards, annealing in Ar at 1000 °C (1 h) was employed for C fiber formation. Conformal TiO_2 coating was carried out at 200 °C using $TiCl_4$ precursor in an ALD reactor (R200 Picosun). The $TiCl_4$ precursor and H_2O reagent were kept at 19 °C and pulsed consecutively with a 10 s purge time in between. Both the $TiCl_4$ and H_2O pulses were 0.1 s while maintaining a N_2 flowing atmosphere of 15 mbar in the reactor. TiO_2 nitridation was achieved by annealing at 750 °C for 8 h in NH_3 atmosphere (10 °C min^{-1} ramps). For the synthesis of Ir NPs on the fibers surface, we dip-coated the fibers in an aqueous solution of $IrBr_3$ (10 mg ml^{-1}), followed by drying at room temperature and heat treatment at 600 °C for 1 h (slow heating and cooling ramps of 2 °C min^{-1} and 3 °C min^{-1}, respectively) in 5% H_2 atmosphere. For SEM imaging and EDX, a ZEISS Auriga instrument was employed, using voltage of 3–5 keV for imaging (InLens detector) and 15–20 keV for spectroscopy. Raman scattering spectra were recorded using a Horiba Jobin-Yvon iHR320 monochromator paired with an Andor i-DUS CCD detector. A near-infrared solid-state laser (785 nm, ∼80 W cm^2) served as the excitation source, and an Olympus LMPLFLN 50× high working distance objective was utilized. FOR ICP-MS, the samples were submerged in 8 ml of boiling aqua regia (3:1 HCl:HNO_3 v/v, concentrated) and subsequently sonicated for 10 min for complete dissolution. This solution was diluted 100-fold with 2% HNO_3, and the Ir concentration was measured with an ICP-MS instrument (Agilent 7900×). The net mass of Ir in the sample was calculated from the concentrations/dilutions.

The sample for scanning transmission electron microscopy (STEM) was prepared by drop-casting an aqueous suspension of the catalyst powder onto a copper-lacey carbon TEM grid (AgarScientific). The STEM measurements were performed on a JEOL-ARM 200CF operated at 80 kV.

Electrochemical characterization was carried out using a GDE setup (GDE cell). Fibers were cut in disks (4 mm diameter) and pressed against a Nafion 115 membrane. The Nafion was previously hydrated by immersing it in milliQ water overnight. A catalyst backing layer of Toray paper (Fuel Cell store) was used to avoid contact between the stainless steel base of the GDE and the electrolyte, preventing parasitic reactions. Humidified N_2 was flown during the measurements. The cell was completed by a fine Pt mesh as a counter electrode and a hydrogen reference electrode, immersed in $HClO_4$ (0.1 M). Electrochemical measurements were conducted using a Biologic SP-150e. Automated 85% IR compensation was adopted based on preliminary impedance measurement (1.55 V bias, 1 MHz to 100 mHz, 10 points/decade, 10 mV oscillation). Additional 15% correction was applied manually. CV curves were recorded between 1 V and 1.65 V, 20 mV s^{-1} rate. Subtraction of capacitive currents was carried out by considering the current values before the OER onset. Before starting the measurements, stabilization of the system was ensured by recording a series of CV measurements during 60 mins. Reference TiO_2 dense films were deposited on sapphire substrate using the same ALD recipe. Electrical conductivity measurements were conducted using a four-probe Van der Pauw configuration in a Linkam probe station.

For XPS analysis, we utilized the Versa Probe 3 AD (Phi, Chanhassen, US) for with a monochromatic Al Kα x-ray source. Each measurement involved acquiring spectra with a 200 μm analysis spot size and a charge neutralizer due to the samples' lack of conductivity. Survey spectra were collected at a pass energy of 224 eV with a step size of 1 eV, whereas HR XPS spectra were captured at a pass energy of 69 eV and a step of 0.05 eV. Surveys consisted of five cycles, and while analyzing HR spectra, ten cycles were collected for each element. We corrected the XPS spectra for charging effects using the carbon C 1s peak at a binding energy (BE) of 284.7 eV. An estimated BE scale accuracy is 0.2 eV; HR analyzes measured elements Ti 2p, C 1s, O 1s, N 1s, Si 2p and Ir 4f.

Data availability statement

The data that support the findings of this study are openly available at the following URL/DOI: https://doi.org/10.5281/zenodo.13850404.

Acknowledgments

This project received funding from the European Union's Horizon 2020 research and innovation program under the Marie Skłodowska-Curie Grant Agreement No. 840787 (Thin-CATALYzER). The authors would also like to acknowledge the Slovenian Research and Innovation Agency (ARIS) within the research Programs P2-0393, P1-0034, P2-0132, I0-0003 and the Projects GC-0004, J1-4401, N2-0248, N2-0423 and J7-4636. We also acknowledge NATO Science for Peace and Security Program (Grant G6230) and the 'CERCA program/Generalitat de Catalunya'.

Author contributions

Federico Baiutti 0000-0001-9664-2486
Conceptualization (lead), Data curation (lead), Formal analysis (lead), Funding acquisition (lead), Investigation (lead), Methodology (lead), Project administration (lead), Resources (lead), Validation (lead), Visualization (lead), Writing – original draft (lead), Writing – review & editing (equal)

Kosova Kreka 0000-0002-7864-2148
Investigation (equal), Methodology (equal), Writing – review & editing (equal)

Aleš Marsel 0009-0002-9462-1432
Investigation (equal), Methodology (equal), Writing – review & editing (equal)

Miha Hotko
Investigation (equal), Methodology (equal), Writing – review & editing (equal)

Marjan Bele
Investigation (equal), Methodology (equal), Writing – review & editing (equal)

Anja Logar
Investigation (equal), Methodology (equal), Writing – review & editing (equal)

Martin Šala 0000-0001-7845-860X
Formal analysis (equal), Investigation (equal), Methodology (equal), Writing – review & editing (equal)

Črtomir Donik 0000-0001-6531-8771
Formal analysis (equal), Investigation (equal), Methodology (equal), Writing – review & editing (equal)

Lazar Bijelić 0009-0007-7474-3236
Formal analysis (equal), Investigation (equal), Methodology (equal), Writing – review & editing (equal)

Carolina Duque Serra
Investigation (equal), Methodology (equal)

Alex Morata 0000-0002-3300-4636
Funding acquisition (equal), Investigation (equal), Writing – review & editing (equal)

Albert Tarancon 0000-0002-1933-2406

Funding acquisition (equal), Project administration (equal), Supervision (equal), Writing – review & editing (equal)

Miran Gaberscek 0000-0002-8104-1693
Funding acquisition (equal), Project administration (equal), Supervision (equal), Validation (equal), Writing – review & editing (equal)

Nejc Hodnik 0000-0002-7113-9769
Funding acquisition (equal), Supervision (lead), Validation (equal), Writing – review & editing (equal)

References

[1] Schmidt O, Gambhir A, Staffell I, Hawkes A, Nelson J and Few S 2017 Future cost and performance of water electrolysis: an expert elicitation study *Int. J. Hydrog. Energy* **42** 30470–92
[2] Carmo I, Cherevko S, Zeradjanin A R and Mayrhofer K J J 2014 Oxygen electrochemistry as a cornerstone for sustainable energy conversion *Angew. Chem., Int. Ed.* **53** 102–21
[3] Trasatti S 2000 Electrocatalysis: understanding the success of DSA® *Electrochim. Acta* **45** 2377–85
[4] Lettenmeier P *et al* 2016 Durable membrane electrode assemblies for proton exchange membrane electrolyzer systems operating at high current densities *Electrochim. Acta* **210** 502–11
[5] Babic U, Suermann M, Büchi F N, Gubler L and Schmidt T J 2017 Critical review—identifying critical gaps for polymer electrolyte water electrolysis development *J. Electrochem. Soc.* **164** F387
[6] Möckl M, Ernst M F, Kornherr M, Allebrod F, Bernt M, Byrknes J, Eickes C, Gebauer C, Moskovtseva A and Gasteiger H A 2022 Durability testing of low-iridium PEM water electrolysis membrane electrode assemblies *J. Electrochem. Soc.* **169** 064505
[7] Chuang M-C and Ho J A 2012 Efficient electrocatalytic oxidation of water: minimization of catalyst loading by an electrostatic assembly of hydrous iridium oxide colloids *RSC Adv.* **2** 4092–6
[8] Lattach Y, Rivera J F, Bamine T, Deronzier A and Moutet J-C 2014 Iridium oxide–polymer nanocomposite electrode materials for water oxidation *ACS Appl. Mater. Interfaces* **6** 12852–9
[9] Huynh T B N, Choi Y, Lee M H, Oh S, Kim M J and Kwon O J 2023 Heat treatment for enhancing Ir-based catalysts enclosed in a carbon layer for electrochemical oxygen evolution reaction *ACS Sustain. Chem. Eng.* **11** 15124–34
[10] Reier T, Nong H N, Teschner D, Schlögl R and Strasser P 2017 Electrocatalytic oxygen evolution reaction in acidic environments—reaction mechanisms and catalysts *Adv. Energy Mater.* **7** 1601275
[11] Tian B, Li Y, Liu Y, Ning F, Dan X, Wen Q, He L, He C, Shen M and Zhou X 2023 Ordered membrane electrode assembly with drastically enhanced proton and mass transport for proton exchange membrane water electrolysis *Nano Lett.* **23** 6474–81
[12] Maass S, Finsterwalder F, Frank G, Hartmann R and Merten C 2008 Carbon support oxidation in PEM fuel cell cathodes *J. Power Sources* **176** 444–51
[13] Fujigaya T, Shi Y, Yang J, Li H, Ito K and Nakashima N 2017 A highly efficient and durable carbon nanotube-based anode electrocatalyst for water electrolyzers *J. Mater. Chem. A* **5** 10584–90
[14] Wen X, Bai L, Li M and Guan J 2018 Ultrafine iridium oxide supported on carbon nanotubes for efficient catalysis of oxygen evolution and oxygen reduction reactions *Mater. Today Energy* **10** 153–60
[15] Xu J, Liu G, Li J and Wang X 2012 The electrocatalytic properties of an IrO2/SnO2 catalyst using SnO2 as a support and an assisting reagent for the oxygen evolution reaction *Electrochim. Acta* **59** 105–12
[16] Li G, Li K, Yang L, Chang J, Ma R, Wu Z, Ge J, Liu C and Xing W 2018 Boosted performance of Ir species by employing TiN as the support toward oxygen evolution reaction *ACS Appl. Mater. Interfaces* **10** 38117–24
[17] Hao C, Lv H, Mi C, Song Y and Ma J 2016 Investigation of mesoporous niobium-doped TiO_2 as an oxygen evolution catalyst support in an SPE water electrolyzer *ACS Sustain. Chem. Eng.* **4** 746–56
[18] Genova-Koleva R V, Alcaide F, Álvarez G, Cabot P L, Grande H-J, Martínez-Huerta M V and Miguel O 2019 Supporting IrO 2 and IrRuOx nanoparticles on TiO 2 and Nb-doped TiO 2 nanotubes as electrocatalysts for the oxygen evolution reaction *J. Energy Chem.* **34** 227–39
[19] Böhm D, Beetz M, Gebauer C, Bernt M, Schröter J, Kornherr M, Zoller F, Bein T and Fattakhova-Rohlfing D 2021 Highly conductive titania supported iridium oxide nanoparticles with low overall iridium density as OER catalyst for large-scale PEM electrolysis *Appl. Mater. Today* **24** 101134
[20] Bele M *et al* 2020 Increasing the oxygen-evolution reaction performance of nanotubular titanium oxynitride-supported Ir nanoparticles by a strong metal-support interaction *ACS Catal.* **10** 13688–700
[21] Chen K, Shen T, Lu Y, Hu Y, Wang J, Zhang J and Wang D 2022 Engineering titanium oxide-based support for electrocatalysis *J. Energy Chem.* **67** 168–83
[22] Kim E J, Kim K H, Bak J, Lee K and Cho E 2022 Carbon nanotube–titanium dioxide nanocomposite support for improved activity and stability of an iridium catalyst toward the oxygen evolution reaction *RSC Adv.* **12** 35943–9
[23] Deng J, Zhang J, Chen J, Luo Y, Chen Y, Xue Y, Wang G and Wang R 2020 Fabrication of layered porous TiO2/carbon fiber paper decorated by Pt nanoparticles using atomic layer deposition for efficient methanol electro-oxidation *J. Electroanal. Chem.* **874** 114468
[24] Wang P, Wen Y, Yin S, Wang N and Shen P K 2017 PtRh alloys on hybrid TiO2–carbon support as high efficiency catalyst for ethanol oxidation *Int. J. Hydrog. Energy* **42** 24689–96
[25] Xia B Y, Wang B, Wu H B, Liu Z, Wang X and (David) Lou X W 2012 Sandwich-structured TiO2–Pt–graphene ternary hybrid electrocatalysts with high efficiency and stability *J. Mater. Chem.* **22** 16499–505
[26] Yue X, Pu Y, Zhang W, Zhang T and Gao W 2020 Ultrafine Pt nanoparticles supported on double-shelled C/TiO2 hollow spheres material as highly efficient methanol oxidation catalysts *J. Energy Chem.* **49** 275–82
[27] Koderman Podboršek G, Zupančič Š, Kaufman R, Surca A K, Marsel A, Pavlišič A, Hodnik N, Dražić G and Bele M 2022 Microstructure and electrical conductivity of electrospun titanium oxynitride carbon composite nanofibers *Nanomaterials* **12** 2177
[28] Morata A, Pacios M, Gadea G, Flox C, Cadavid D, Cabot A and Tarancón A 2018 Large-area and adaptable electrospun silicon-based thermoelectric nanomaterials with high energy conversion efficiencies *Nat. Commun.* **9** 4759

[29] Loncar A, Moriau L, Stojanovski K, Ruiz-Zepeda F, Jovanovic P, Bele M, Gaberscek M and Hodnik N 2020 Ir/TiONx/C high-performance oxygen evolution reaction nanocomposite electrocatalysts in acidic media: synthesis, characterization and electrochemical benchmarking protocol *J. Phys. Energy* **2** 02LT01
[30] Omer S, Forgách L, Zelkó R and Sebe I 2021 Scale-up of electrospinning: market overview of products and devices for pharmaceutical and biomedical purposes *Pharmaceutics* **13** 286
[31] Feng Y *et al* 2024 Comprehensive evaluation of commercially scalable atomic-layer-deposited alumina coating impact on full cell battery performance across varied test conditions *J. Energy Storage* **100** 113711
[32] Muñoz-Rojas D and MacManus-Driscoll J 2014 Spatial atmospheric atomic layer deposition: a new laboratory and industrial tool for low-cost photovoltaics *Mater. Horiz.* **1** 314–20
[33] Gong C, Yan C, Zhang J, Cheng X, Pan H, Zhang C, Yu L and Zhang Z 2011 Room-temperature ferromagnetism evolution in nanostructured titanium nitride superconductors—the influence of structural defects *J. Mater. Chem.* **21** 15273–8
[34] El-Deen S S, Hashem A M, Abdel Ghany A E, Indris S, Ehrenberg H, Mauger A and Julien C M 2018 Anatase TiO_2 nanoparticles for lithium-ion batteries *Ionics* **24** 2925–34
[35] Parker J C and Siegel R W 1990 Calibration of the Raman spectrum to the oxygen stoichiometry of nanophase TiO2 *Appl. Phys. Lett.* **57** 943–5
[36] Lewinski K A, van der Vliet D and Luopa S M 2015 NSTF advances for PEM electrolysis—the effect of alloying on activity of NSTF electrolyzer catalysts and performance of NSTF based PEM electrolyzers *ECS Trans.* **69** 893
[37] Fabreguette F, Imhoff L, Maglione M, Domenichini B, Marco de Lucas M C, Sibillot P, Bourgeois S and Sacilotti M 2000 Correlation between the electrical properties and the morphology of low-pressure MOCVD titanium oxynitride thin films grown at various temperatures *Chem. Vap. Depos.* **6** 109–14
[38] Fàbrega C, Andreu T, Güell F, Prades J D, Estradé S, Rebled J M, Peiró F and Morante J R 2011 Effectiveness of nitrogen incorporation to enhance the photoelectrochemical activity of nanostructured TiO2:NH3 versus H2–N2 annealing *Nanotechnology* **22** 235403
[39] Polfus J M, Norby T and Haugsrud R 2013 The defect chemistry of nitrogen in oxides: a review of experimental and theoretical studies *J. Solid State Chem.* **198** 65–76
[40] Watzele S, Hauenstein P, Liang Y, Xue S, Fichtner J, Garlyyev B, Scieszka D, Claudel F, Maillard F and Bandarenka A S 2019 Determination of electroactive surface area of Ni-, Co-, Fe-, and Ir-based oxide electrocatalysts *ACS Catal.* **9** 9222–30
[41] Schröder J, Mints V A, Bornet A, Berner E, Fathi Tovini M, Quinson J, Wiberg G K H, Bizzotto F, El-Sayed H A and Arenz M 2021 The gas diffusion electrode setup as straightforward testing device for proton exchange membrane water electrolyzer catalysts *JACS Au.* **1** 247–51
[42] Majsztrik P, Bocarsly A and Benziger J 2008 Water permeation through Nafion membranes: the role of water activity *J. Phys. Chem. B* **112** 16280–9
[43] Alia S M, Rasimick B, Ngo C, Neyerlin K C, Kocha S S, Pylypenko S, Xu H and Pivovar B S 2016 Activity and durability of iridium nanoparticles in the oxygen evolution reaction *J. Electrochem. Soc.* **163** F3105
[44] Li G, Jia H, Liu H, Yang X and Lin M-C 2022 Nanostructured IrOx supported on N-doped TiO2 as an efficient electrocatalyst towards acidic oxygen evolution reaction *RSC Adv.* **12** 28929–36
[45] Hu W, Chen S and Xia Q 2014 IrO2/Nb–TiO2 electrocatalyst for oxygen evolution reaction in acidic medium *Int. J. Hydrog. Energy* **39** 6967–76
[46] Shinagawa T, Garcia-Esparza A T and Takanabe K 2015 Insight on Tafel slopes from a microkinetic analysis of aqueous electrocatalysis for energy conversion *Sci. Rep.* **5** 13801
[47] Fang Z *et al* 2024 Doped TiO2-supported IrO2 electrocatalysts with high activity and durability toward the acidic oxygen evolution reaction *CrystEngComm* **26** 475–83